Consistent high order meshfree Galerkin methods and applications

†Qinglin Duan*, Bingbing Wang, Xin Gao, Xikui Li and Hongwu Zhang

The State key Laboratory of Structural Analysis for Industrial Equipment, Department of Engineering Mechanics, Dalian University of Technology, Dalian, Liaoning 116024, P.R.China.

*Presenting author: qinglinduan@dlut.edu.cn
†Corresponding author: qinglinduan@dlut.edu.cn

Abstract

Meshfree methods such as the element-free Galerkin (EFG) method have been developed to be a formidable competitor and also a beneficial complement to the traditional finite element method (FEM) which dominates engineering analysis for decades. One attractive advantage of meshfree methods is that constructing high order approximation is much more convenient than that in the finite element method (FEM). However, high order meshfree methods are computationally inefficient since a large number of integration points are required. On the other hand, the stabilized conforming nodal integration method based on strain smoothing is very efficient for linear meshfree Galerkin methods, but it cannot exploit the high convergence and accuracy of meshfree methods with high order approximation. In this work, the number of quadrature points for high order meshfree methods is remarkably reduced by correcting the nodal derivatives. Such correction is rationally developed based on the Hu-Washizu three-field variational principle. The proposed method is able to exactly pass patch tests in a consistent manner and is therefore, named as consistent high order meshfree Galerkin methods. In contrast, the traditional meshfree methods cannot exactly pass patch tests. Numerical results of elastostatic problems show that the proposed technique remarkably improves the numerical performance of high order meshfree methods in terms of accuracy, convergence, efficiency and stability. Applications of the proposed methods to thin plates and shells as well as crack problems are also presented.

Keywords: Meshfree; EFG; Numerical integration; Plate; Shell; Crack

Introduction

Meshfree methods[1-6] such as the element-free Galerkin (EFG) method developed in recent twenty years have become a formidable competitor to the traditional finite element method (FEM) which dominates engineering analysis for decades. The common feature shared by the so called “meshfree” or “meshless” methods is that they are based on scattered data approximation which do not need explicit nodal connectivity(element). So far, EFG is one of the most popular and successful meshfree methods. Its fundamental advantage against traditional FEM is the smoothness of the approximation function. With careful choice of the weight function for the MLS process, the continuity of the approximation function can be C^{∞} which provides superiority for solving high order partial differential equation such as thin plates and shells whereas the continuity of the FEM approximation is only C^{0}. Furthermore, high order approximation can be conveniently obtained in EFG. The required change in the input data is minimum. In contrast, in FEM, high order elements such as 6-node or 10-node triangle elements have to be constructed and this changes the input data a lot. Finally, EFG is easy to achieve h-adaptive computation[7] since its approximation is only based on nodes (not elements).

However, a main issue of the EFG method (or more generally the meshfree methods) is the efficient numerical integration of the weak form. Background meshes with Gauss integration points are commonly used in EFG. Due to the non-polynomial character of the MLS approximants, high order Gauss integration has to be employed to result a stable method. Clearly, the large number of integration points consumes more CPU time and thus severely impairs the computational efficiency. What’s worse is that even the high order integration cannot integrate the weak form accurately enough to make the method exactly pass the patch test.

Many efforts have been devoted to develop stable and efficient integration methods with reduced number of sampling points such as the nodal integration [8-10], the stress-point

integration [11-12], the support domain integration [13], etc. Among these, the nodal integration initiated by Bessial and Belytschko [8] can dramatically improve the efficiency since it uses the minimum evaluating points (the nodes) as integration points. However, direct nodal integration is not stable and can't pass the patch tests, some works have been done to relieve this issue [10-15]. Among these, Chen *et al.* [14] developed a stabilized conforming nodal integration (SCNI) which is stable and provides even better accuracy than Gauss integration. They showed that SCNI can pass the linear patch test whereas Gauss integration fails. One outstanding merit of this method is that no additional term or stabilization parameter is involved. So far, SCNI has developed to be a major integration scheme in meshfree method and the strain smoothing technique in SCNI has been extend into FEM analysis [16].
However, Puso *et.al.* [17] reported SCNI may still cause oscillation near the boundary of the solution domain. What is more, Duan *et.al.* [18] reported that SCNI is only linear exactness and is not adequate for quadratic meshfree approximation. They further presented a consistency framework guiding the correction of the nodal derivatives based on the divergence theorem between a nodal shape function and its derivatives to remedy this issue. Particularly, a three-point integration scheme with second order accuracy named quadratically consistent three-point (QC3) integration method for second order meshfree method is developed in such framework. QC3 employs triangular background integration cells. In each integration cell, the nodal shape functions on six boundary sampling points and three domain sampling points are used to determinate the nodal corrected derivatives on the three domain sampling points. Later, by further reformulating the framework of nodal derivative correction based on the Hu-Washizu three-field variational principle, Duan *et.al.* [19] proposed the consistent element-free Galerkin (CEFG) method and showed its much better numerical performance in terms of accuracy, convergence, efficiency and stability than the standard EFG method. It should be stressed that the proposed EFG method is based on the Hu-Washizu three-field variational principle and can pass the patch tests in a consistent manner, i.e. EFG with linear, quadratic and cubic bases can, respectively, pass the linear, quadratic and cubic patch tests. Therefore, the method is named as consistent element-free Galerkin (CEFG) method. In contrast, the traditional EFG method is based on the classical one-field variational principle and cannot pass the patch tests.
The paper is structured as follows. The standard EFG method is first reviewed in section 2. The proposed consistent EFG method is then described in section 3. Applications of the proposed method to thin-plates and shells as well as crack problems are presented in section 4 followed by the conclusions in section 5.

Element-free Galerkin (EFG) method: approximation and discretization

EFG was invented by Belytschko *et al.* [2] about twenty years ago and so far it has already developed into one of the most popular and successful meshfree Galerkin methods. Consider a two dimensional elastostatic problem in the domain $\Omega \subset \mathbf{R}^2$ with a set of nodes $\mathbf{X}_I$, the displacement $\mathbf{u}(\mathbf{x})$ at an arbitrary point $\mathbf{x}$ is approximated in a form similar to that in FEM

$$\mathbf{u}^h(\mathbf{x}) = \mathbf{N}(\mathbf{x})\mathbf{U} = \sum_I \mathbf{N}_I(\mathbf{x})\mathbf{U}_I \tag{1}$$

where $\mathbf{U}$ is the unknown vector of nodal displacement parameters. $\mathbf{N}(\mathbf{x})$ is the matrix of nodal shape functions

$$\mathbf{u}^h(\mathbf{x}) = \mathbf{N}(\mathbf{x})\mathbf{U} = \sum_I \mathbf{N}_I(\mathbf{x})\mathbf{U}_I \tag{2}$$

The nodal shape function $N_I(\mathbf{x})$ is constructed by MLS and can be written as

$$N_I(\mathbf{x}) = \mathbf{p}^{\mathrm{T}}(\mathbf{X}_I) w_I(\mathbf{x}) \boldsymbol{\alpha}(\mathbf{x}) \tag{3}$$

where $\mathbf{p}(\mathbf{x})$ is a vector of base functions which usually includes a complete basis of the polynomials to a given order, $w_I(\mathbf{x})$ a weight function and $\boldsymbol{\alpha}(\mathbf{x})$ the unknown vector. The unknown vector $\boldsymbol{\alpha}(\mathbf{x})$ can be determined by the so called reproducibility condition, i.e. the consistency condition

$$\mathbf{p}(\mathbf{x}) = \sum_I \mathbf{p}(\mathbf{X}_I) N_I(\mathbf{x}) \tag{4}$$

Substitution of Eq.(3) into Eq.(4) leads to

$$\mathbf{A}(\mathbf{x})\boldsymbol{\alpha}(\mathbf{x}) = \mathbf{p}(\mathbf{x}) \tag{5}$$

where

$$\mathbf{A}(\mathbf{x}) = \sum_I \mathbf{p}(\mathbf{X}_I)\mathbf{p}^{\mathrm{T}}(\mathbf{X}_I) w_I(\mathbf{x}) \tag{6}$$

The nodal MLS shape functions $N_I(\mathbf{x})$ can be obtained from Eq.(3) after the unknown vector $\boldsymbol{\alpha}(\mathbf{x})$ is solved from Eq.(5). Computation of the derivatives of the MLS shape functions is by taking the derivative of Eq.(3)

$$N_{I,i}(\mathbf{x}) = \mathbf{p}^{\mathrm{T}}(\mathbf{X}_I)\left[w_{I,i}(\mathbf{x})\boldsymbol{\alpha}(\mathbf{x}) + w_I(\mathbf{x})\boldsymbol{\alpha}_{,i}(\mathbf{x}) \right] \tag{7}$$

where subscripts preceded by commas denote partial derivatives with respect to spatial coordinates. The unknown $\boldsymbol{\alpha}_{,i}(\mathbf{x})$ in Eq.(7) can be solved from the derivative of Eq.(6)

$$\mathbf{A}(\mathbf{x})\boldsymbol{\alpha}_{,i}(\mathbf{x}) = \mathbf{p}_{,i}(\mathbf{x}) - \mathbf{A}_{,i}(\mathbf{x})\boldsymbol{\alpha}(\mathbf{x}) \tag{8}$$

with

$$\mathbf{A}_{,i}(\mathbf{x}) = \sum_I \mathbf{p}(\mathbf{X}_I)\mathbf{p}^{\mathrm{T}}(\mathbf{X}_I) w_{I,i}(\mathbf{x}) \tag{9}$$

For a elastostatic problem on a 2D domain Ω bounded by Γ, EFG uses the classical displacement variational principle to construct the weak form $\delta\Pi(\mathbf{u})$, i.e

$$\delta\Pi(\mathbf{u}) = \int_\Omega \delta\boldsymbol{\varepsilon}^{\mathrm{T}}\mathbf{D}\boldsymbol{\varepsilon}\,\mathrm{d}\Omega - \int_{\Gamma_t} \delta\mathbf{u}^{\mathrm{T}}\bar{\mathbf{t}}\,\mathrm{d}\Gamma - \int_\Omega \delta\mathbf{u}^{\mathrm{T}}\mathbf{b}\,\mathrm{d}\Omega \tag{10}$$

where $\mathbf{D}$ is the material modulus, prefix δ denotes a variation and the strain is

$$\boldsymbol{\varepsilon} = \begin{bmatrix} \varepsilon_{xx} & \varepsilon_{yy} & \gamma_{xy} \end{bmatrix}^{\mathrm{T}} = \begin{bmatrix} \dfrac{\partial u}{\partial x} & \dfrac{\partial v}{\partial y} & \dfrac{\partial u}{\partial y} + \dfrac{\partial v}{\partial x} \end{bmatrix}^{\mathrm{T}} = \mathbf{B}\mathbf{U} = \sum_I \mathbf{B}_I \mathbf{U}_I \tag{11}$$

with

$$\mathbf{B} = \begin{bmatrix} \mathbf{B}_1 & \mathbf{B}_2 & \cdots & \mathbf{B}_n \end{bmatrix} \quad \text{and} \quad \mathbf{B}_I = \begin{bmatrix} \dfrac{\partial N_I}{\partial x} & 0 \\ 0 & \dfrac{\partial N_I}{\partial y} \\ \dfrac{\partial N_I}{\partial y} & \dfrac{\partial N_I}{\partial x} \end{bmatrix} \tag{12}$$

By taking the variation, the following discretized equation can be obtained

$$\mathbf{K}\mathbf{U} = \mathbf{f} \tag{13}$$

where

$$\mathbf{K} = \int_\Omega \mathbf{B}^{\mathrm{T}}\mathbf{D}\mathbf{B}\,\mathrm{d}\Omega \qquad \mathbf{f} = \int_\Omega \mathbf{N}^{\mathrm{T}}\mathbf{b}\,\mathrm{d}\Omega + \int_{\Gamma_t} \mathbf{N}^{\mathrm{T}}\bar{\mathbf{t}}\,\mathrm{d}\Gamma \tag{14}$$

Consistent integration schemes for high order approximation

Consistent element-free Galerkin methods (CEFG) proposed by Duan *et.al.* [19] can pass patch tests exactly and consistently. This is due to special integration schemes with corrected nodal derivatives are developed for EFG methods. The computation of the corrected nodal derivatives is based on the divergence theorem and it starts form the following equation:

$$\int_{\Omega_S} \tilde{N}_{I,i}(\mathbf{x})\mathbf{q}(\mathbf{x})\mathrm{d}\Omega = \int_{\Gamma_S} N_I(\mathbf{x})\mathbf{q}(\mathbf{x})n_i\mathrm{d}\Gamma - \int_{\Omega_S} N_I(\mathbf{x})\mathbf{q}_{,i}(\mathbf{x})\mathrm{d}\Omega \tag{15}$$

where $\tilde{N}_{I,i}(\mathbf{x})$ is the corrective derivatives, Ω_S bounded by Γ_S the cell for domain integration, $\mathbf{q}(\mathbf{x})$ the base obtained by

$$\mathbf{q}(\mathbf{x}) = \mathbf{p}_{,x}(\mathbf{x}) \cup \mathbf{p}_{,y}(\mathbf{x}) = \left[q_1(\mathbf{x}) \quad q_2(\mathbf{x}) \quad \cdots \quad q_m(\mathbf{x})\right]^{\mathrm{T}} \tag{16}$$

Using the divergence theorem to the right term of Eq.(15) leads to

$$\int_{\Omega_S} \tilde{N}_{I,i}(\mathbf{x})\mathbf{q}(\mathbf{x})\mathrm{d}\Omega = \int_{\Omega_S} N_{I,i}(\mathbf{x})\mathbf{q}(\mathbf{x})\mathrm{d}\Omega \tag{17}$$

Considering the $\mathbf{q}(\mathbf{x})$ is the base of the assumed Cauchy stress $\hat{\boldsymbol{\sigma}}$ space, Eq.(17) can be further rewritten as

$$\int_{\Omega_S} \hat{\boldsymbol{\sigma}}^{\mathrm{T}}\left(N_{I,i} - \tilde{N}_{I,i}\right)\mathrm{d}\Omega = \mathbf{0} \tag{18}$$

Since the corrective derivatives used for domain integrations represent the assumed strain, Eq.(18) can be replaced by:

$$\int_{\Omega_S} \hat{\boldsymbol{\sigma}}^{\mathrm{T}}(\boldsymbol{\varepsilon} - \tilde{\boldsymbol{\varepsilon}})\mathrm{d}\Omega = \mathbf{0} \tag{19}$$

The above equation shows that the nodal corrected derivatives satisfy the orthogonality condition which means the nodal corrected derivative formulation can be derived from the Hu-Washizu three-field variational principle rational. The according consistent integration schemes are designed based on the numerical integration form of Eq.(15) with triangular integration cells as

$$\sum_{D=1}^{n_\Omega} W_D \frac{\partial \tilde{N}_I(\mathbf{x}_D)}{\partial x_i}\mathbf{q}(\mathbf{x}_D) = \sum_{e=1}^{3}\sum_{b=1}^{n_\Gamma} w_b N_I(\mathbf{x}_b)\mathbf{q}(\mathbf{x}_b)n_i^e - \sum_{D=1}^{n_\Omega} W_D N_I(\mathbf{x}_D)\mathbf{q}_{,i}(\mathbf{x}_D) \tag{20}$$

where W_D and w_b are, respectively, the integration weights of the evaluation points $\mathbf{x}_D$ in cells and $\mathbf{x}_b$ on edges, n_i^e the unit normal to the edge e. For linear, quadratic and cubic meshfree approximation, the following one, three and six integration schemes are designed [19] based on Eq.(20) as showed in Figure 1.

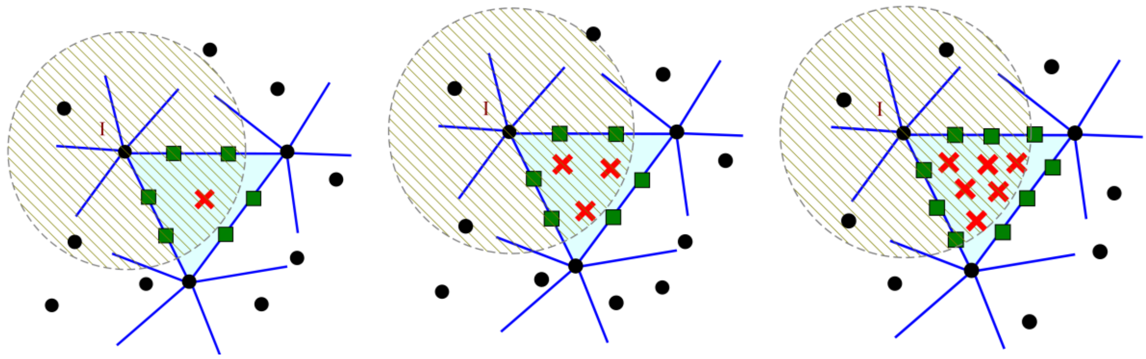

(a) (b) (c)

Figure 1. Schematic diagram of integration schemes for (a) Linear CEFG; (b) Quadratic CEFG and (c) Cubic CEFG; Dark dots denote approximation nodes, red crosses denote evaluation points for domain integration and green squares denote evaluation points for contour integration.

Once nodal corrected derivatives at the domain quadrature points are obtained, the discretized equation based on the Hu-Washizu variational principle is:

$$\tilde{\mathbf{K}}\mathbf{U} = \mathbf{f} \tag{21}$$

where

$$\tilde{\mathbf{K}} = \int_{\Omega} \tilde{\mathbf{B}}^{\mathrm{T}} \mathbf{D} \tilde{\mathbf{B}} \mathrm{d}\Omega \qquad \mathbf{f} = \int_{\Omega} \mathbf{N}^{\mathrm{T}} \mathbf{b} \mathrm{d}\Omega + \int_{\Gamma_t} \mathbf{N}^{\mathrm{T}} \bar{\mathbf{t}} \mathrm{d}\Gamma \tag{22}$$

$$\tilde{\mathbf{B}} = \begin{bmatrix} \tilde{\mathbf{B}}_1 & \tilde{\mathbf{B}}_2 & \cdots & \tilde{\mathbf{B}}_n \end{bmatrix} \quad \text{and} \quad \tilde{\mathbf{B}}_I^{\mathrm{T}} = \begin{bmatrix} \dfrac{\partial \tilde{N}_I}{\partial x} & 0 & \dfrac{\partial \tilde{N}_I}{\partial y} \\ 0 & \dfrac{\partial \tilde{N}_I}{\partial y} & \dfrac{\partial \tilde{N}_I}{\partial x} \end{bmatrix} \tag{23}$$

Numerical examples

Patch tests

Patch tests [19] are first investigated on a 2×2 domain with 5×5 nodes with irregular nodal distribution. Table 1, Table 2 and Table 3, respectively, compare the numerical results obtained by linear, quadratic and cubic approximations. It is observed that the proposed CEFG methods can pass patch tests in a consistent manner, i.e. linear CEFG is able to pass linear patch test, quadratic CEFG is able to pass up to quadratic patch test and cubic CEFG is able to pass up to cubic patch test. In contrast, the EFG methods fail to pass any patch test both in displacement and in energy.

Table 1 Patch test results: Linear methods

		Linear Patch Test	**Quadratic Patch Test**	**Cubic Patch test**
Linear EFG	E^{disp}	0.37E-06	0.75E-01	0.21E+00
	E^{eng}	0.33E-05	0.23E+00	0.53E+00
Linear CEFG	E^{disp}	0.35E-12	0.36E-01	0.13E+00
	E^{eng}	0.24E-11	0.16E+00	0.44E+00

Table 2 Patch test results: Quadratic methods

		Linear Patch Test	**Quadratic Patch Test**	**Cubic Patch test**
Quadratic EFG	E^{disp}	0.48E-05	0.91E-05	0.26E-01
	E^{eng}	0.36E-04	0.42E-04	0.97E-01
Quadratic CEFG	E^{disp}	0.27E-12	0.43E-12	0.19E-01
	E^{eng}	0.23E-11	0.16E-11	0.78E-01

Table 3 Patch test results: Cubic methods

		Linear Patch Test	**Quadratic Patch Test**	**Cubic Patch test**
Cubic EFG	E^{disp}	0.23E-04	0.99E-05	0.21E-05
	E^{eng}	0.15E-03	0.35E-04	0.59E-05
Cubic CEFG	E^{disp}	0.14E-11	0.85E-12	0.44E-12
	E^{eng}	0.72E-11	0.27E-11	0.13E-11

Pressurized hollow cylinder

A hollow cylinder subjected to internal and external pressure as shown in Figure 2a is examined. As shown in Figure 2b, due to two-fold symmetry, only the first quadrant is modeled.

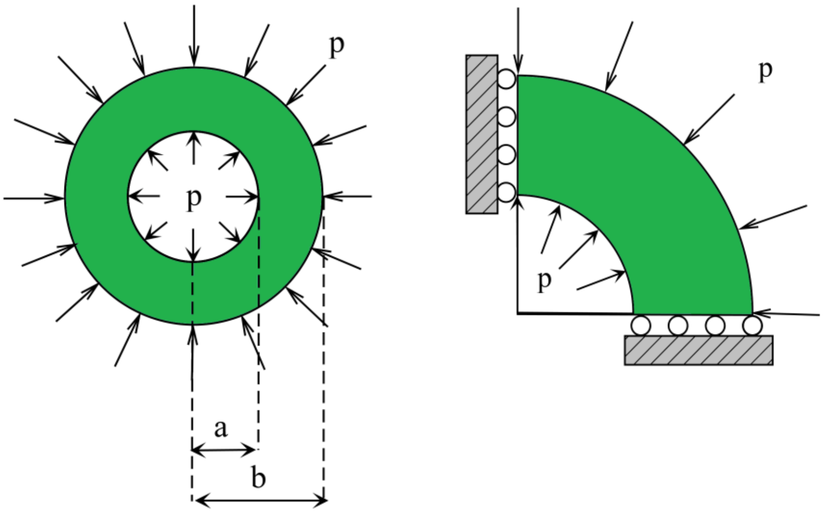

(a) (b)

Figure 2. Plate with a hole problem: (a) schematic diagram; (b) solution domain

Five regular grids with the typical size of the discretization $h = 0.25, 0.2, 0.125, 0.1, 0.0625$ are employed in convergence study and the results are plotted in Figure 3. The proposed CEFG shows better accuracy and convergence rate than EFG both in displacement and in energy. Figure 4 compares the computational efficiency of displacement and energy. The proposed CEFG is much more efficient than standard EFG since less integration points are used. Figure 5 shows the $\sigma_{yy,y}$ fields obtained by the six methods. Clearly, the proposed cubic CEFG method obtains the best $\sigma_{yy,y}$ field which is very smooth. In contrast, considerable oscillations present in the result of the cubic EFG method. The $\sigma_{yy,y}$ fields given by quadratic CEFG and quadratic EFG methods are similar. Same observation is applied to linear CEFG and linear EFG methods.

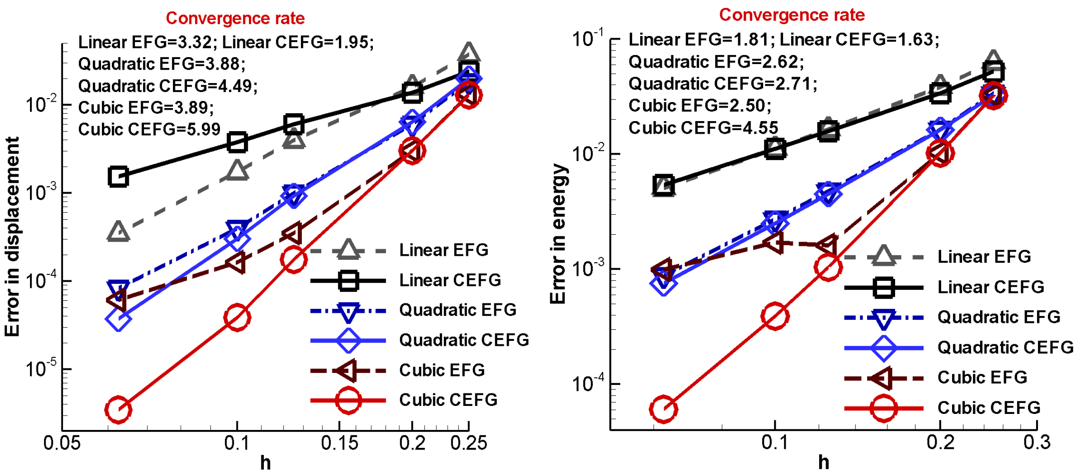

(a) (b)

Figure 3. Convergence of the plate with a hole problem: (a) displacement; (b) energy

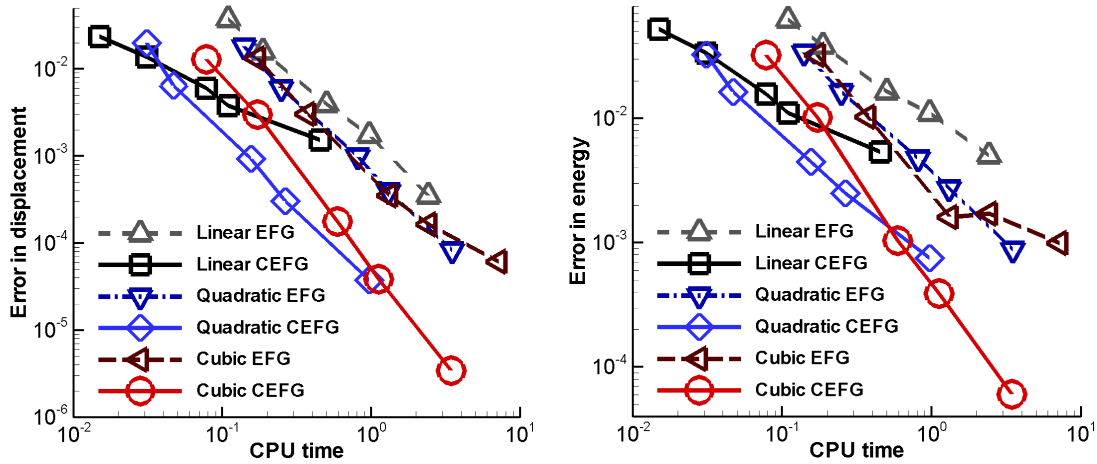

(a) (b)

Figure 4. Computational efficiency of the plate with a hole problem: (a) displacement; (b) energy

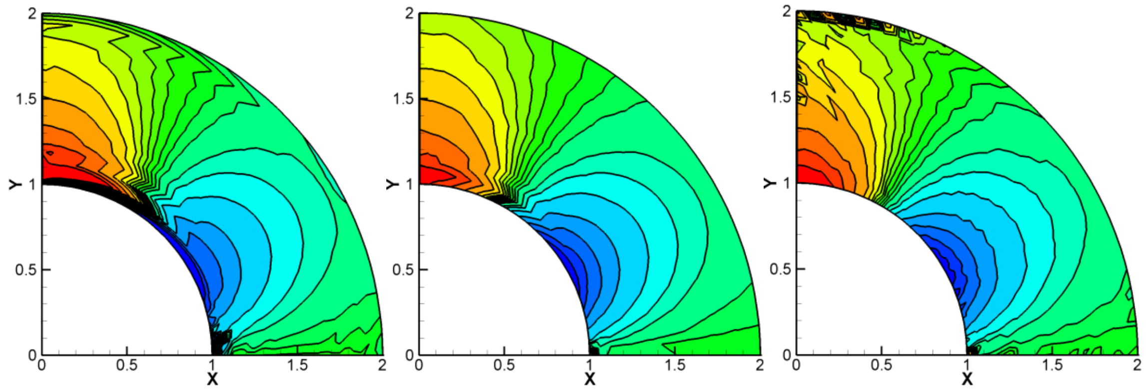

(a) (b) (c)

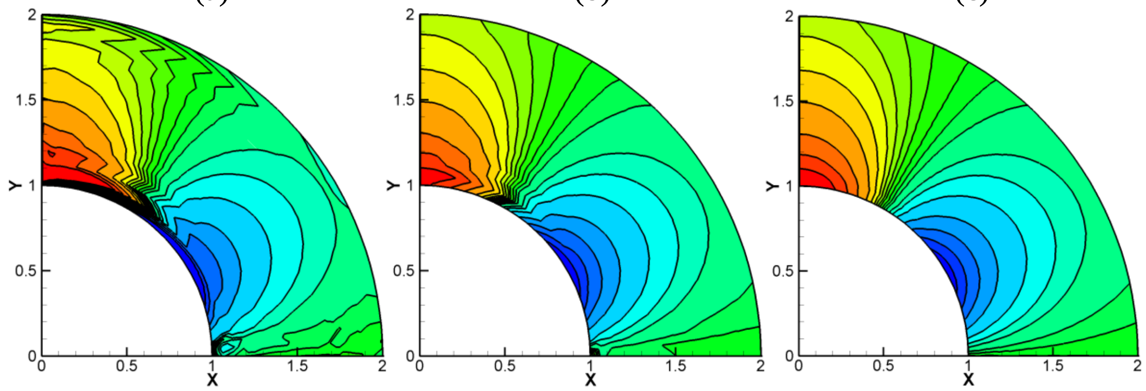

(d) (e) (f)

Figure 5. Comparison of $\sigma_{yy,y}$ fields of the pressurized hollow cylinder problem obtained by: (a) Linear EFG; (b) Quadratic EFG; (c) Cubic EFG;(d) Linear CEFG; (e) Quadratic CEFG; (f) Cubic CEFG.

Application to thin plates and shells

Due to the high smoothness of the meshfree approximations, various works for thin-plate and –shell problems [20-26] have been investigated by meshfree methods. However, high order quadratures are commonly employed to evaluate the Galerkin weak form, which is computationally expensive. In this section, consistent element-free Galerkin method is further extended into thin-plates and thin-shells problems. For such high-order differential equations, cubic approximation is employed in this section.

Thin plates

Since the government equation of thin plates problem is a fourth-order partial differential equation, the kernel idea is to correct the nodal second order derivatives which leads to a curvature smoothing(CS) formulation. The consistent curvature smoothing formulation in each integration cell Ω_k is as follows:

$$\begin{aligned}\int_{\Omega_k} \tilde{N}_{I,\alpha\beta}\mathbf{q}(\mathbf{x})\mathrm{d}\Omega = &\int_{\Gamma_k} \frac{1}{2}\left[N_{I,\alpha}\mathbf{q}(\mathbf{x})n_\beta + N_{I,\beta}\mathbf{q}(\mathbf{x})n_\alpha\right]\mathrm{d}\Gamma \\ &-\int_{\Gamma_k} \frac{1}{2}N_I\left[\mathbf{q}_{,\beta}(\mathbf{x})n_\alpha + N\mathbf{q}_{,\alpha}(\mathbf{x})n_\beta\right]\mathrm{d}\Gamma \\ &-\int_{\Omega_k} N_I\mathbf{q}_{,\alpha\beta}(\mathbf{x})\mathrm{d}\Omega\end{aligned} \tag{24}$$

For cubic meshfree approximation which leads to a linear curvature smoothing(LCS) formulation, the above equation reduces to:

$$\begin{aligned}&\int_{\Omega_k} \tilde{N}_{I,\alpha\beta}\mathrm{d}\Omega = \int_{\Gamma_k} \frac{1}{2}\left(N_{I,\alpha}n_\beta + N_{I,\beta}n_\alpha\right)\mathrm{d}\Gamma \\ &\int_{\Omega_k} \tilde{N}_{I,\alpha\beta}x\mathrm{d}\Omega = \int_{\Gamma_k} \frac{1}{2}x\left(N_{I,\alpha}n_\beta + N_{I,\beta}n_\alpha\right)\mathrm{d}\Gamma - \int_{\Gamma_k} \frac{1}{2}N_I\left(\delta_1^\beta n_\alpha + \delta_1^\alpha n_\beta\right)\mathrm{d}\Gamma \\ &\int_{\Omega_k} \tilde{N}_{I,\alpha\beta}y\mathrm{d}\Omega = \int_{\Gamma_k} \frac{1}{2}y\left(N_{I,\alpha}n_\beta + N_{I,\beta}n_\alpha\right)\mathrm{d}\Gamma - \int_{\Gamma_k} \frac{1}{2}N_I\left(\delta_2^\beta n_\alpha + \delta_2^\alpha n_\beta\right)\mathrm{d}\Gamma\end{aligned} \tag{25}$$

Eq.(25) are used to correct the nodal second order derivatives.

Numerical examples

A square with four simply supported edges under uniform load

As showed in Figure 6, a 1×1 square subjected to uniform load with the magnitude $q=1$ is tested. The four edges of the square are simply supported. The Young's modules and the Poission ratio are $E=1\times10^{10}$ and $\nu=0.3$. The thickness of the plate is $t=0.001$.

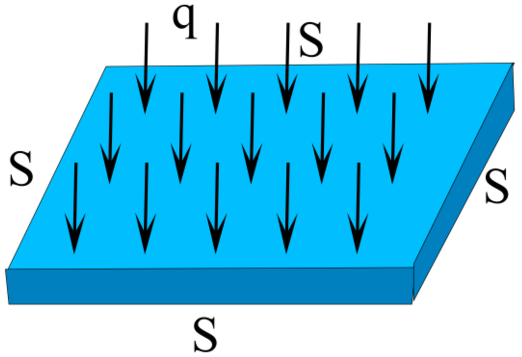

Figure 6. A square with four simply supported edges under uniform load

Four irregular grids are used for convergence study in this problem and the results are showed in Figure 7. The proposed LCS achieves the highest accuracy for both deflection and energy. Figure 8 shows the efficiency results of the deflection and energy. It is observed that the proposed LCS is the most efficiency method for both deflection and energy.

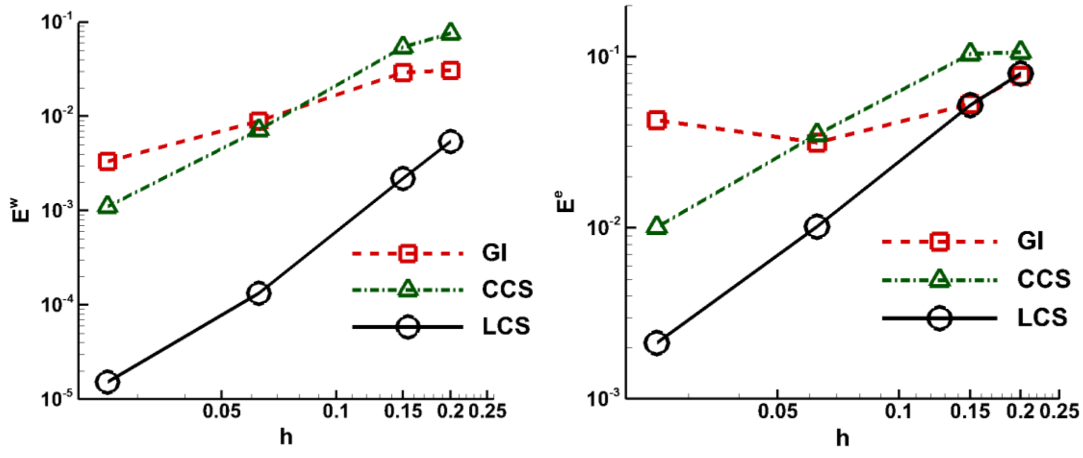

(a) (b)

Figure 7. Convergence of the square with four simply supported edges under uniform load problem: (a) deflection; (b) energy.

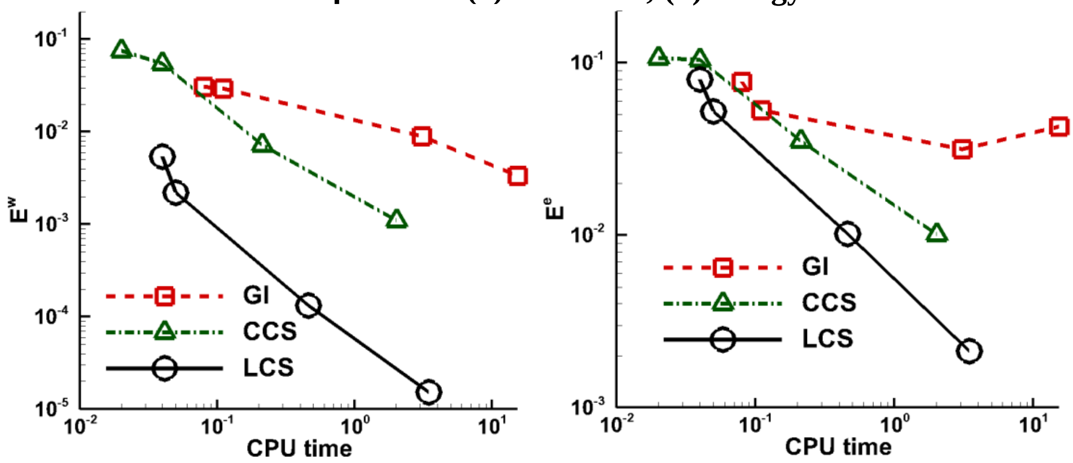

(a) (b)

Figure 8. Efficiency of a square with four simply supported edges under uniform load problem: (a) deflection; (b) energy

Simply supported circular plate under uniform load

A circular simply supported plate under uniform load as shown in Figure 9 is next investigated. The radius of the plate is $R = 2$ and the thickness of the plate is $t = 0.001$.Material parameters are the Young's modules $E = 1\times10^{10}$ and Poission ratio $v = 0.3$. The magnitude of applied uniform load is $q = 0.1$.

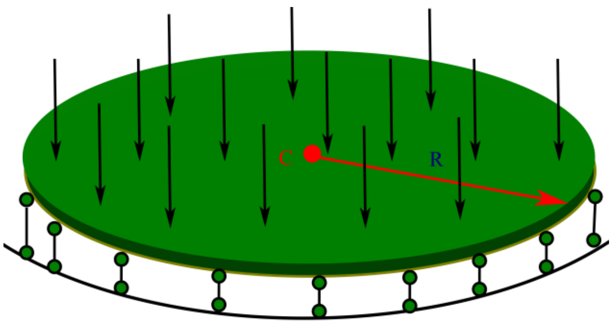

Figure 9. Simply supported circular plate under uniform load

The full model is used for analysis with three grids containing 168, 414 and 1547 nodes, respectively. The convergence of the deflection of the center point w_C is showed in figure 10. It is clearly that the proposed LCS agrees best with the exact solution.

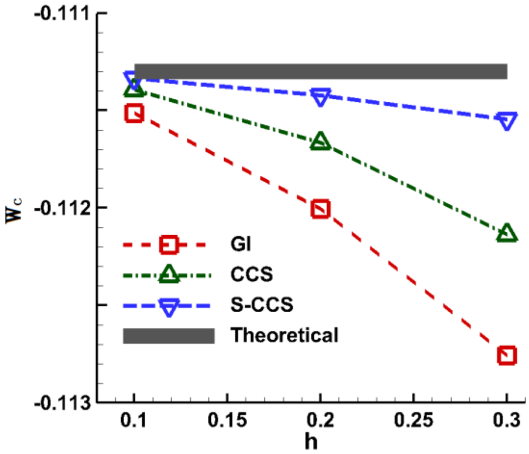

Figure 10. The convergence result of the deflection of the center point w_C

Thin shells problem

The geometrically exact thin shell model [26] is considered in this paper. A linear strain smoothing formulation is proposed in parametric space for thin shell analysis which contains the membrane strain smoothing and curvature smoothing:

$$\int_{\mathscr{A}_S} \tilde{N}_{I,\alpha}(\xi)\mathbf{q}(\xi)d\mathscr{A}_S = \int_{\partial\mathscr{A}_S} N_I(\xi)\mathbf{q}(\xi)n_\alpha dl_\xi - \int_{\mathscr{A}_S} N_I(\xi)\mathbf{q}_{,\alpha}(\xi)d\mathscr{A}_S \tag{26}$$

$$\int_{\mathscr{A}_S} \tilde{N}_{I,\alpha\beta}(\xi)\mathbf{q}(\xi)d\mathscr{A}_S = \int_{\partial\mathscr{A}_S} N_{I,\alpha}(\xi)\mathbf{q}(\xi)n_\beta dl_\xi - \int_{\mathscr{A}_S} N_{I,\alpha}(\xi)\mathbf{q}_{,\beta}(\xi)d\mathscr{A}_S \tag{27}$$

where $\mathscr{A}_S$ is the background integration cell in parametric space. $\mathbf{q}(\xi)$ is chosen as a linear base of the parametric space $\mathscr{A}$:

$$\mathbf{q}(\xi) = \begin{pmatrix} 1 \\ \xi^1 \\ \xi^2 \end{pmatrix} \tag{28}$$

Numerical examples

Pinched hemispherical shell with 18° *hole*

Hemispherical shell problem is tested. The hemispherical has an 18° hole at the top. The thickness of the shell is $h=0.04$ and the radius $R=10$. The material parameters contain Young's modulus $E=6.825e7$ and Poisson's ratio $v=0.3$. The shell is subjected to two pairs of load which are equal and opposite along the X- and Y- axes.

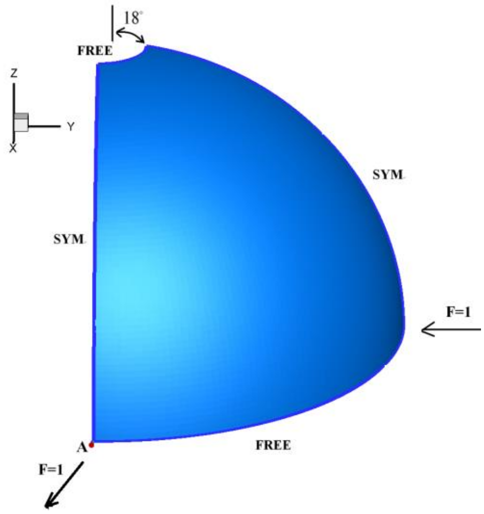

Figure 11. Schematic diagram of hemispherical shell with 18° **hole problem**

Due to the symmetry, only a quarter of the geometry is modelled, see figure 11. The convergence result is shown in figure 12. It can be seen that the proposed method agrees well with the reference solution and performs better than GI-16 and CCS with the densest node configuration.

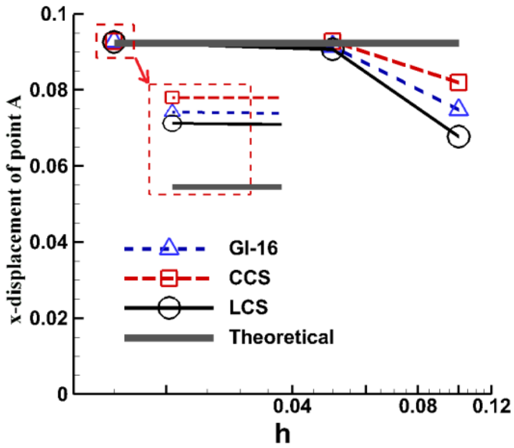

Figure 12. Convergence of the X-displacement of point A

Scordelis-Lo roof

The Scordelis-Lo roof problem [26] is a benchmark problem for a curved shell analysis. The geometrical parameter of the roof are: the length $L=50$, the radius $R=25$, the thickness $h=0.25$ and the span angle $\theta=80^{\circ}$. The material properties are: Young's modulus $E=4.32\text{e}8$ and the Poisson ratio $v=0$. The roof is loaded by a self-weight $q=90$. The model is fixed by two opposite rigid diaphragms and the other two edges are free. Four irregular grids with 36, 121, 441 and 1684 nodes are employed for the convergence study and the convergence curves are presented in Figure 13.

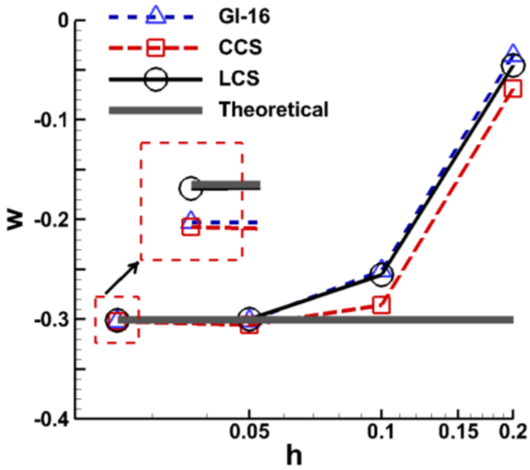

Figure 13. Convergence of the mid-side vertical displacements of Scordelis-Lo roof problem

Figure 14 shows the contours of membrane stress n_{12} by GI-16, CCS and LCS. The proposed LCS achieves smoothed contour while mildly spurious oscillations are observed by GI-16 and CCS. Figure 15 shows the contours of bending stress m_{11} by GI-16, CCS and LCS. GI-16 results severely spurious oscillations although it uses the most quadrature points. LCS achieves much better bending stress m_{11} contour, but mild oscillations still appear. Only the proposed LCS results smoothed bending stress m_{11} contour. This shows the superiority of the proposed LCS.

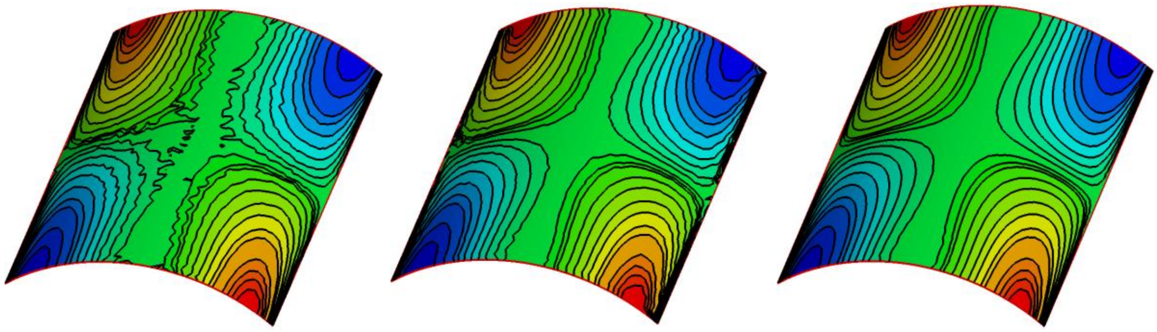

(a) (b) (c)

Figure 14. Membrane stress n_{12} contour of Scordelis-Lo roof problem by: (a) GI-16; (b) CCS; (c) LCS

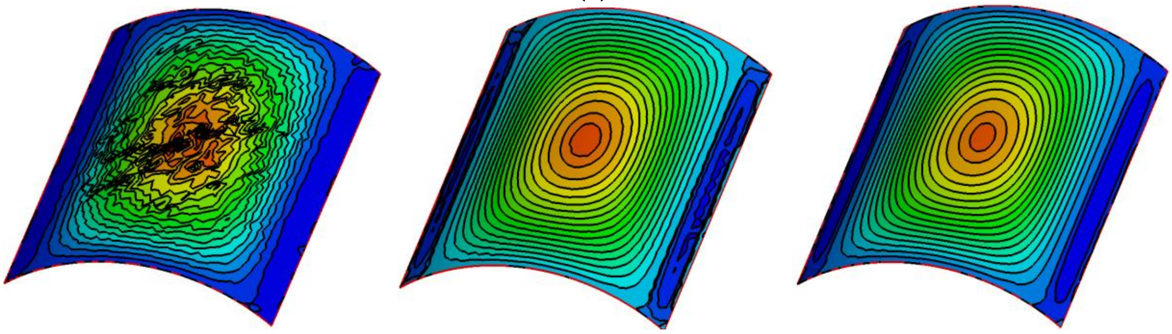

(a) (b) (c)

Figure 15. Bending stress m_{11} contour of Scordelis-Lo roof problem by: (a) GI-16; (b) CCS; (c) LCS

Application to crack problems

The method has been developed to deal with a problem of linear elastic fracture mechanics. There is no enrichment function for the discontinuous displacement field.

Crack description

A phantom-node method[27] is developed to describe cracks. We start with the discontinuous displacement field in an element

$$u(\mathbf{x}) = \sum_{I=1} N_I(\mathbf{x})\left\{\mathbf{u}_I + \mathbf{q}_I\left[H\left(f(\mathbf{x})\right) - H\left(f(\mathbf{x}_I)\right)\right]\right\} \tag{29}$$

where $H(\cdot)$ is the Heaviside step function given by

$$H(x) = \begin{cases} 1 & \forall x > 0 \\ 0 & \forall x \le 0 \end{cases} \tag{30}$$

and $f(\mathbf{x}) = 0$ represents the position of the crack. So, Eq.(29) are subdivided each term into parts that are associated with $f(\mathbf{x}) < 0$ and $f(\mathbf{x}) > 0$, we have

$$\mathbf{u} = \sum_{I=1}\left[(\mathbf{u}_I - \mathbf{q}_I)H_I^+ N_I(1-H) + \mathbf{u}_I H_I^- N_I(1-H) + \mathbf{u}_I H_I^+ N_I H + (\mathbf{u}_I + \mathbf{q}_I)H_I^- N_I H\right] \tag{31}$$

If we then let

$$\mathbf{u}_I^1 = \begin{cases} \mathbf{u}_I & f(\mathbf{x}_I) < 0 \\ \mathbf{u}_I - \mathbf{q}_I & f(\mathbf{x}_I) > 0 \end{cases} \tag{32}$$

$$\mathbf{u}_I^2 = \begin{cases} \mathbf{u}_I + \mathbf{q}_I & f(\mathbf{x}_I) < 0 \\ \mathbf{u}_I & f(\mathbf{x}_I) > 0 \end{cases} \tag{33}$$

We can write the displacement field as

$$\mathbf{u}(\mathbf{x}) = \sum_{I \in S_1} \mathbf{u}_I^1 N_I(\mathbf{x}) H(-f(\mathbf{x})) + \sum_{I \in S_2} \mathbf{u}_I^2 N_I(\mathbf{x}) H(f(\mathbf{x})) \tag{34}$$

where S_1 and S_2 are the index sets of the relative nodes of superposed element 1 and 2, respectively. As can be seen from Figure 16, each element contains original real nodes and phantom nodes.

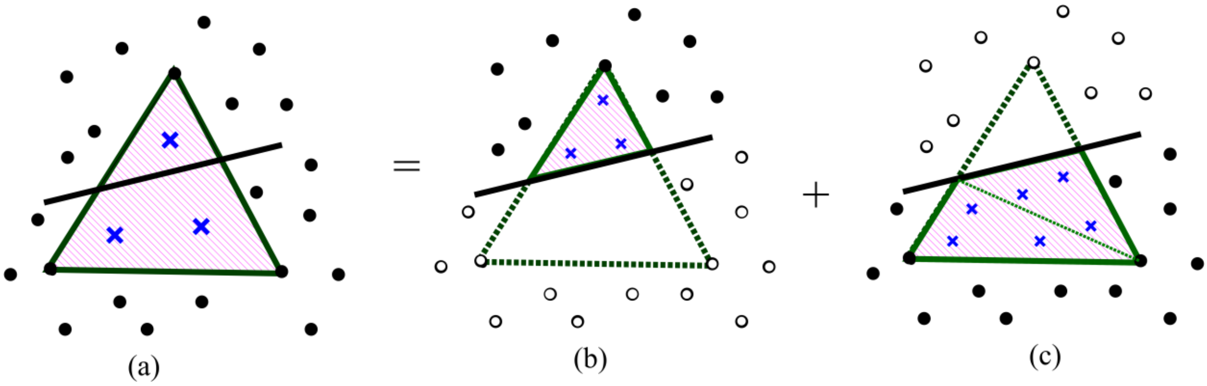

Figure 16 The decomposition of a cracked element into two elements

Therefore, elements are overlapped on the position of the crack, and they are partially integrated to implement the discontinuous displacement across the crack.

Numerical examples

The discontinuous patch test

This example was devised by Dolbow and Devan[28]. Shown in Figure.17 is a 3×3 square domain that is subjected to a discontinuous horizontal traction with $t = 10$. It is assumed that the domain is completely bisected into two regions by the failure surface(i.e. red line).

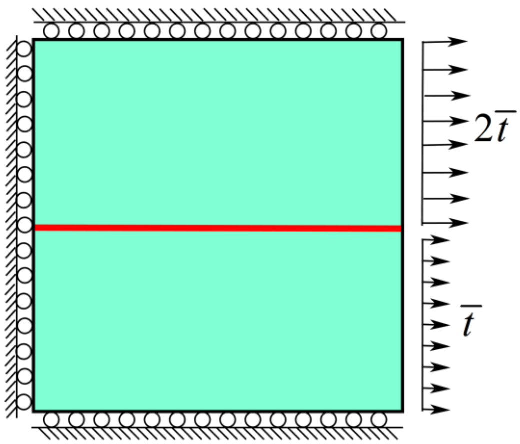

Figure.17 Schematic diagram of the discontinuous patch test configuration and loading

A 4×4 grid is used for analysis. The distributions of σ_{xx} are shown in Figure.18 for compressible case and incompressible case, respectively. The results suggest that the method can exactly pass the test in the both cases.

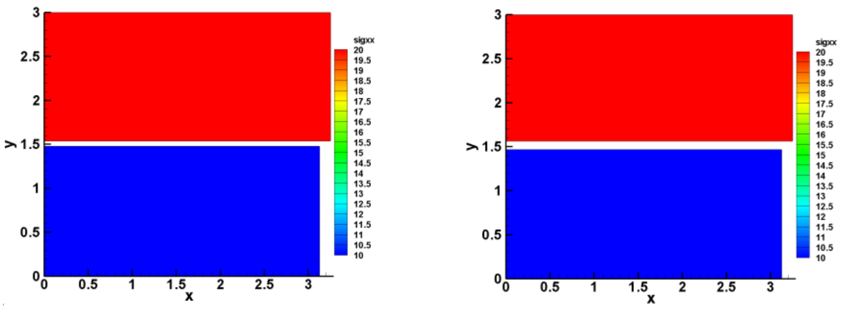

Figure. 18 σ_{xx} distribution of: (a) compressible case ;(b) incompressible case

Edge cracked plates under tension or shear

Consider a plane stress plate of width $b=7$ and height $l=16$ with an edge crack length of $a=b/2=3.5$. The material properties are $E=10^7$, and $\nu=0.3$.The plate is subjected to a tension $\sigma=1$ at the top(see Figure.19a) or sustains a shear $\tau=1$ on the top edge(see Figure.19b).

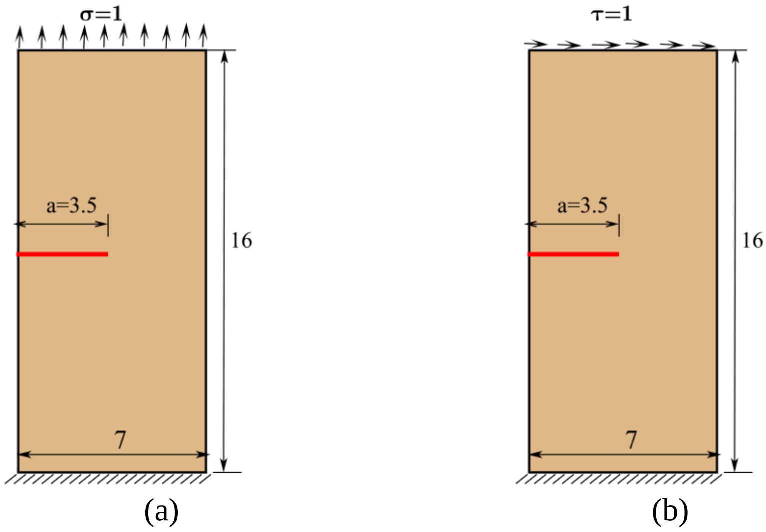

Figure.19 Schematic diagram of the edge cracked plate under:(a) tension; (b) shear

The analytical solution for the plate under tension is given by

$$K_I = F(\lambda)\sigma\sqrt{\pi a} \tag{35}$$

with $F(\lambda)=1.12-0.231\lambda+10.55\lambda^2-21.72\lambda^3+30.39\lambda^4$.The values of K_I and K_{II} for the shear case in [29] are used as the reference solution:

$$K_I = 34.0,\ K_{II} = 4.55 \tag{36}$$

Table.4 The results of normalized K_I and K_{II}

Cases	EFG		CEFG	
	K_I	K_{II}	K_I	K_{II}
Tension case	1.067	--	1.008	--
Shear case	1.062	0.991	1.005	0.998

A 30×71 regular grid is used for the evaluating of stress intensity factors. Table.4 lists the evaluating results of normalized K_I and K_{II} with two methods for tension case and shear case, respectively. The results show that CEFG method is able to give more accurate stress intensity factors than the standard EFG method.

Crack growth from a fillet

This example shows the growth of a crack from a fillet in a structural member. The experiment to be modelled is shown in Figure.20, with the computational domain outlined with a dashed line. The material properties are $E = 200Gpa$, and $\nu = 0.3$, respectively. The applied load is $P = 1.0N$. The initial crack length is $a_0 = 5mm$. To model a very thick beam, the displacement is fixed along the entire bottom of the computational domain, that is, rigid constraint. A flexible constraint is idealized to model a very thin beam.

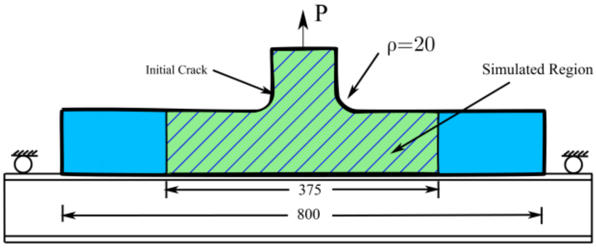

Figure.20 Experimental configuration and simulated region for a fillet problem

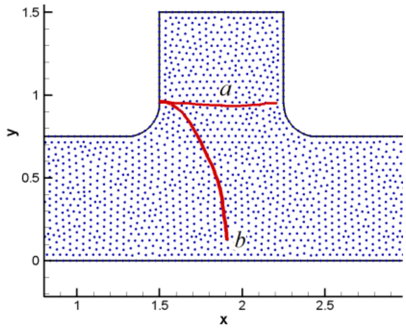

Figure.21 Crack growth paths of two different constraints: a. Flexible constraint; b. Rigid constraint

This experiment is presented in Reference [30] to investigate the effect of the thickness of the lower I-beam on crack growth. Figure.21 shows the crack paths predicted by the proposed method for a thick I-beam and a thin I-beam, respectively. These results agree well with the experimental results [30].

Conclusions

Consistent element-free Galerkin method and its applications are presented. For elastostatic solids, CEFG performs much better than standard EFG in terms of accuracy, convergence and efficiency, according to the numerical results. Application of the high order CEFG method to thin plates and shells as well as crack problems is also presented. It is demonstrated that the CEFG method is really promising in these applications.

Acknowledgement

The authors are pleased to acknowledge the support of this work by Science Challenge Project (No. JCKY2016212A502), the National Key Research and Development Program of China (2016YFC1402705, 2016YFC1402706), the National Natural Science Foundation of China (11372066, 11232003), the Fundamental Research Funds for the Central Universities (DUT15LK07), the open funds of the state key laboratory of water resources and hydropower engineering science (2015SGG03), the open funds of the state key laboratory of Geohazard Prevention and Geoenvironment Protection (SKLGP2016K007).

References

[1] Nayroles B, Touzot G, Villon P. (1992) Generalizing the finite element methods: Diffuse approximation and diffuse elements. *Computational Mechanics* **10**, 307-318.

[2] Belytschko T, Lu YY, Gu L. (1994) Element-free Galerkin methods. *International Journal for Numerical Methods in Engineering* **37**, 229–256.

[3] Liu W.K., Jun S, Zhang Y.F. (1994) Reproducing kernel particle methods. *International Journal for Numerical Methods in Fluids* **20**, 1081–1106.

[4] Duarte CA, Oden JT. (1996) H-p clouds—an h-p meshless method. *Numer. Methods Partial Differ. Equations* **12**, 673-705.

[5] Zhang X. (2001) Least-Squares collocation meshless method. *International Journal for Numerical Methods in Engineering* **51**, 1089–1100.

[6] Liu GR, Gu YT and Dai K. (2004) Assessment and applications of point interpolation methods for computational mechanics, *International Journal for Numerical Methods in Engineering* 59, 1373-1397.

[7] Rabczuk T, Belytschko T. (2005) Adaptivity for structured meshfree particle methods in 2D and 3D. *International Journal for Numerical Methods in Engineering* **63**, 1559–1582.

[8] Dolbow J, Belytschko T. (1999) Numerical integration of the Galerkin weak form in meshfree methods. *Computational Mechanics* **23**, 219–230.

[9] Beissel S, Belytschko T. (1996) Nodal integration of the element-free Galerkin method. *Computer Methods in Applied Mechanics and Engineering* **139**, 49–74.

[10] Liu GR, Zhang GY, Wang YY, Zhong ZH, Li GY, Han X. (2007) A nodal integration technique for meshfree radial point interpolation method (NI-RPIM). *International Journal of Solids and Structures* **44**, 3840–3860.

[11] Dyka CT, Randles PW, Ingel RP. (1997) Stress points for tension instability in SPH. *International Journal for Numerical Methods in Engineering* **40**, 2325–2341.

[12] Fries TP, Belytschko T. (2008) Convergence and stabilization of stress-point integration in mesh-free and particle methods. *International Journal for Numerical Methods in Engineering* **74**, 1067–1087.

[13] Liu Y, Belytschko T. (2010) A new support integration scheme for the weak form in mesh-free methods. *International Journal for Numerical Methods in Engineering* **82**, 699–725.

[14] Chen JS, Wu CT, Yoon S, You Y. (2001) A stabilized conforming nodal integration for Galerkin mesh-free methods. *International Journal for Numerical Methods in Engineering* **50**, 435–466.

[15] G. Y. Zhang, G. R. Liu, Y. Y. Wang H. T. Huang, Z. H. Zhong, G. Y. Li and X. Han. (2007) A linearly conforming point interpolation method (LC-PIM) for three-dimensional elasticity problems. *International Journal for Numerical Methods in Engineering* **72**, 1524-1543.

[16] Liu G, Dai K, Nguyen T. (2007) A smoothed finite element method for mechanics problems. *Computational Mechanics* **39**, 859-877.

[17] Puso MA, Chen JS, Zywicz E, Elmer W. (2008) Meshfree and finite element nodal integration methods. *International Journal for Numerical Methods in Engineering* **74**, 416–446.

[18] Duan QL, Li XK, Zhang HW, Belytschko T. (2012) Second-order accurate derivatives and integration schemes for meshfree methods. *International Journal for Numerical Methods in Engineering* **92**, 399–424.

[19] Duan QL, Gao X, Wang BB et.al. (2014) Consistent element-free Galerkin method. *International Journal for Numerical Methods in Engineering* **99**, 79–101.

[20] Krysl P, Belytschko T. (1995) Analysis of thin plates by the element-free Galerkin method. *Computational Mechanics* **17**, 26–35.

[21] Cui X, Liu G, Li G et.al. (2011) A thin plate formulation without rotation DOFs based on the radial point interpolation method and triangular cells. *International Journal for Numerical Methods in Engineering* **85**, 958–986.

[22] Chen JS, Wang D. (2006) A constrained reproducing kernel particle formulation for shear deformable shell in Cartesian coordinate. *International Journal for Numerical Methods in Engineering* **68**, 151–172.

[23] Wang D, Chen JS. (2008) A Hermite reproducing kernel approximation for thin-plate analysis with sub-domain stabilized conforming integration. *International Journal for Numerical Methods in Engineering* **74**, 368–390.

[24] Krysl P, Belytschko T. (1996) Analysis of thin shells by the element-free Galerkin method. *International Journal of Solids and Structures* **33**, 3057-3080.

[25] Rabczuk T, Areias P, Belytschko T. (2007) A meshfree thin shell method for non-linear dynamic fracture. *International Journal for Numerical Methods in Engineering* **72**, 524–548.

[26] Millan D, Rosolen A, Arroyo M. (2011) Thin shell analysis from scattered points with maximum-entropy approximations. *International Journal for Numerical Methods in Engineering* **85**, 723–751.

[27] Song J.H., Areias P. M. A. and Belytschko T.(2006) A method for dynamic crack and shear band propagation with phantom nodes, *Int. J. Numer. Meth. Engng* **67**, 868–893.

[28] Dolbow J, Devan A.(2004) Enrichment of enhanced assumed strain approximations for representing strong discontinuities: addressing volumetric incompressibility and the discontinuous patch test. *Int J Numer Methods Eng*, **59**:47–67.

[29] Yau J.F., Wang S.S., Corten H.T. (1980) A mixed-mode crack analysis of isotropic solids using conservation laws of elasticity. *J Appl Mech ASME* **47**,335-341.

[30] Sumi Y., Yang C., Wang Z. N. (1996) Morphological aspects of fatigue crack propagation. Part II—effects of stress biaxiality and welding residual stress. *International Journal of Fracture* **82**(3), 221-235.